Planetary and Space Science 59 (2011) 227–237

Contents lists available at ScienceDirect

Planetary and Space Science

journal homepage: www.elsevier.com/locate/pss

# Atmospheric modeling of Mars methane surface releases

Michael A. Mischna [a,*], Mark Allen [a,1], Mark I. Richardson [b,2], Claire E. Newman [b,2], Anthony D. Toigo [c,3]

[a] Jet Propulsion Laboratory, California Institute of Technology, 4800 Oak Grove Dr., M/S 183-401, Pasadena, CA 91109, USA
[b] Division of Geological and Planetary Sciences, California Institute of Technology, MC 150-21, 1200 E. California Blvd. Pasadena, CA 91125, USA
[c] Cornell University, Department of Astronomy, Ithaca, NY 14853, USA

ARTICLE INFO

*Article history:*
Received 21 January 2010
Received in revised form
11 May 2010
Accepted 1 July 2010
Available online 7 July 2010

*Keywords:*
Mars atmosphere
Methane
Plumes
MarsWRF
General circulation model

ABSTRACT

We utilize the MarsWRF general circulation model (GCM) to address the behavior of gas plumes in the Martian atmosphere, with the specific goal of characterizing the source of the recently identified methane detection in the Martian atmosphere. These observations have been interpreted as the release of methane from localized surface sources with spatial and temporal variabilities. Due to the limited temporal coverage of ground-based observations, we use a GCM to simulate the development of passive atmospheric plumes over relevant timescales. The observations can be reproduced best if the release occurred just before the time of observation—no more than 1–2 sols earlier—and if this release were nearly instantaneous rather than a slow, steady emission. Furthermore, it requires a source region spanning a broad latitudinal range rather than a point emission. While the accuracy of our conclusions about this specific methane release scenario is limited by the uncertainties inherent in GCM simulations of the Martian atmosphere, our findings regarding generalized plume behavior are robust, and illustrate the potential power of numerical modeling for constraining plume source conditions.



## 1. Introduction

The recent putative discovery of methane in the Martian atmosphere hints at a planet far more active than once thought. As a reduced gas in an oxidizing atmosphere, methane will not survive in the atmosphere for long (standard photochemical models predict a lifetime of only 350 yr), and its continued presence therefore requires an active, or at least somewhat recent, emission source. Sources of atmospheric methane can potentially derive from both biotic and abiotic sources. A proven biotic source would be the first confirmation of Martian life to date. Abiotic sources, such as seepage from subsurface reservoirs of methane (from clathrate decomposition, serpentinization or volcanic processes) might offer insights to extant habitable subsurface zones.

The earliest reports of Martian atmospheric methane (Krasnopolsky et al., 2004; Formisano et al., 2004) both suggested mean values of ~10 ppb. The ground-based survey by Krasnopolsky captured only a portion of the Martian disk, while the Mars Express Planetary Fourier Spectrometer (PFS) observations of Formisano summed a wide range of latitude and longitude. More recent investigations (Krasnopolsky, 2007; Geminale et al., 2008) have yielded disparate findings. In the former, ground-based, study, a $3\sigma$ upper limit of 14 ppb methane was established, but only valid for the time of observation (northern spring, $L_s = 9^\circ$), while the latter study, based on a broad range of PFS observations of the 3018 $cm^{-1}$ methane line, showed evidence of widespread temporal and spatial variability in the methane signal, from 5–60+ ppb. Recent work by Mumma et al. (2009) (hereafter M09) applied infrared spectroscopic techniques to search for Martian methane in the 3.3 μm spectral band, and identified multiple spectral lines having both spatial and temporal variabilities on the scale of several Mars years.

The distinct spatial variability reported in M09 suggests local source regions, while the temporal variability suggests possible seasonal variations in the source strength and, more surprisingly, extremely rapid destruction of methane through non-photochemical processes. Based upon the strength and estimated size of the strongest observed methane plume, the emission rate was estimated to be at least 0.6 kg $s^{-1}$, generating a mean mixing ratio of ~33 ppb over the region of influence (approximately 60° in diameter) with a peak mixing ratio of ~45 ppb (ref. M09, Fig. 2c, curve d), and little methane outside this region. Were the contents of this plume to be spread uniformly over the globe, it would equate with a global average mixing ratio of ~2 ppb. Combined with other seasonally contiguous plumes that were also measured, the total global average methane abundance was estimated to be 6 ppb. However, observations of the following Martian year

* Corresponding author. Tel.: +1 818 393 4775; fax: +1 818 393 4445.
*E-mail addresses:* michael.a.mischna@jpl.nasa.gov (M.A. Mischna), mark.a.allen@jpl.nasa.gov (M. Allen), mir@ashimagroup.net (M.I. Richardson), claire@ashimagroup.net (C.E. Newman), toigo@astro.cornell.edu (A.D. Toigo).
[1] Also, Division of Geological and Planetary Sciences, California Institute of Technology, MC 150-21, 1200 E. California Blvd. Pasadena, CA 91125, USA
[2] Present address: Ashima Research, 600 S. Lake Ave, Suite 303, Pasadena, CA 91106, USA
[3] Present address: The Johns Hopkins University, Applied Physics Laboratory, 11100 Johns Hopkins Rd., Laurel, MD 20723, USA

0032-0633/$ - see front matter © 2010 Elsevier Ltd. All rights reserved.
doi:10.1016/j.pss.2010.07.005

found a mean mixing ratio of only 3 ppb; thus M09 concluded that the chemical lifetime of atmospheric methane on Mars had to be less than ~4 Mars years, and possibly as short as ~200 sols—far shorter than the 350-year photochemical lifetime previously assumed. The conclusion that was drawn, then, was that methane is being removed from the atmosphere through means substantially more efficient that photochemical processes alone.

M09 provided some limited analysis of plume evolution over time based upon the assumption of a diffusion-only atmosphere. (We will show that diffusion makes only a minor contribution to the dispersal of a methane plume.) A subsequent study by Lefèvre and Forget (2009) employed a more sophisticated Martian atmospheric simulation to investigate the question of methane destruction timescales. Neither of these studies, however, has sought to identify the source location of the observed atmospheric methane signals under reasonably realistic atmospheric conditions. Our goal in this work is to apply an advanced Martian atmospheric circulation model to identify or at least constrain the source and emission conditions of the M09 observations. We first wish to address, in a more general sense, however, the behavior of chemical plumes in the present-day Martian atmosphere, and the sensitivity of simulated plume behavior to the model itself. Given a basic understanding of how generic plumes behave under contemporary Martian conditions, we will apply this knowledge to interpreting the M09 observations of methane. Despite the limited amount of observational data available, it may still be possible to place constraints on the timing, location and dimensions of methane source regions to ensure consistency with the M09 observations, given the uncertainties of a specific model simulation. The solution space bounded by these GCM results will provide a good starting point for future directed methane searches by ground-based and orbital techniques by providing a narrowed range of source locations of positively identified release events, and an improved ability to link newly observed plumes back to potential sources.

Section 2 provides the reader with an introduction to the MarsWRF GCM. Section 3 discusses the behavior of generic plumes in the Martian atmosphere as simulated by MarsWRF, while Section 4 evaluates the specific assumptions used in M09 and places additional constraints on the timing, location and duration of the methane sources responsible for the observed signals. This is followed by discussion and interpretation in Section 5, and conclusions in Section 6.

## 2. The MarsWRF general circulation model

The Mars Weather Research and Forecasting (MarsWRF) GCM is a Mars-specific configuration of the PlanetWRF GCM detailed in Richardson et al. (2007); thus, only a brief overview will be presently given. MarsWRF is a finite difference gridpoint model projected onto an Arakawa-C grid with a user-defined horizontal and vertical resolution. In the present study MarsWRF is typically run with a latitude × longitude resolution of $1.25^\circ \times 1.25^\circ$ ($288 \times 144$ grid points, ~75 km resolution at the equator) and 40 vertical levels (0–~80 km altitude) on a modified sigma (terrain-following) vertical coordinate. Additional tests, where indicated, have been run with resolution as coarse as $5^\circ \times 5^\circ$ ($72 \times 36$ grid points, 300 km resolution at the equator). The total, present-day atmospheric $CO_2$ budget has been tuned to fit the Viking Lander annual pressure curves, both surface albedo and thermal inertia are matched to TES observations (Christensen et al., 2001; Putzig et al., 2005), while a MOLA topography base map is employed, and scaled down to the chosen model resolution. Atmospheric radiative transfer is simplified by using a wide-band model consisting of IR absorption in the broad 15 μm band only (Hourdin et al., 1992; Forget et al., 1999). Such a simplification has been shown to yield sufficiently accurate results for the present-day Mars atmosphere. High-frequency waves are removed at latitudes poleward of 60° by a Fourier filtering scheme. MarsWRF includes a water cycle that is passive except for ice-albedo effects (deposition of water ice will increase the surface albedo), however this, and interactions with the Martian subsurface such as soil adsorption, are not considered here. The MarsWRF model employs a third-order Runge-Kutta transport integration scheme that is conservative, but does not guarantee positive definite values for tracer abundance. It is possible, though uncommon, to encounter negative tracer mixing ratios; they are typically encountered in regions of sharp gradients, and thus are most prevalent early in model runs, disappearing within the first few sols. These limited, transient negative values are tolerated to ensure overall tracer mass conservation.

Tests of the dynamical core of MarsWRF show that it produces results that compare favorably to other Mars GCMs when implementing simplified Held-Suarez-like "standard" (Held and Suarez, 1994) model physics. At the Second International Workshop on Mars Atmosphere Modeling and Observations in Granada, Spain, in March 2006, the Seventh International Conference on Mars in Pasadena, California, in July 2007, and the Mars Atmospheric Modeling and Observation Workshop in Williamsburg, Virginia, in November 2008, model intercomparisons were performed between several different Mars GCMs, including MarsWRF, to study their ability to reproduce observed fields in the Martian atmosphere (Wilson, personal communication; Mischna and Wilson, 2008). Comparisons to existing Mars climate models and vertical profiles of TES data showed that MarsWRF is able to replicate key features of the Martian atmosphere quite well. Additional comparisons to TES temperature data (Smith et al., 2001) show a high degree of similarity to observations (Richardson et al., 2007).

MarsWRF is modular and designed to be highly parallelizable, making it both fast and easy to modify. The ability to independently track multiple atmospheric tracers is native to the model, and allows for the simultaneous visualization of tracer evolution for varying setups. Plume releases of varying character can be controlled by the user through modification of four independent tracer parameters in MarsWRF:

(1) *Source location and season*—tracer emission events can be prescribed to occur anywhere, and of any size, in the model, from point sources to regional or global sources. The model season for the simulation can also be adjusted to simulate any time of year.
(2) *Emission duration*—a plume may emit evenly throughout the simulation, for brief periods ('pulses'), or intermittently. The emission history of a plume source can be adjusted as required to simulate quick release episodes or slow, steady outgassing events. Release is assumed to be constant within each prescribed emission period.
(3) *Source strength*—The user can define the magnitude of the release in one of several ways—as a fixed mass (kg), as a surface flux ($kg/m^2/s$) or as a fixed mixing ratio (kg/kg), among others. The release magnitude can vary within the source region. Once in the atmosphere, these tracers do not modify the background atmosphere, thus plumes having the same initial conditions, but different source strengths will evolve identically, scaled only by their relative strengths (e.g., doubling the source flux will result in atmospheric abundances twice as large).

(4) *Tracer lifetime*—the lifetime of the emitted species can be modified to allow the rate of exponential decay of the tracer to be representative of any desired species, or to study the distribution of a tracer with an assigned lifetime. Over time, the abundance of a species will decrease due to this decay, unless replenished from an active source.

For our simulations, the MarsWRF GCM is initialized for 30 model sols (1 sol=1 Martian day) to allow a settling of the atmosphere during model spinup and to produce an initial 'start' file for our subsequent simulations. The tracer is injected into the atmosphere on the 31st sol, and the model stepped forward for a designated period, depending on the parameters chosen for the particular simulation. We have chosen a 'baseline' simulation in late northern summer ($L_s=155^\circ$) to be consistent with the season of the peak methane observation by M09 and to ensure we capture the seasonal weather patterns experienced at these locations at this time of year. The model timestep is set to 60 s to avoid the types of Courant–Friedrichs–Lewy violations that can be experienced at high latitudes with longer time steps. There are no indications of such violations in any of our model runs. At the highest resolution used in this study, MarsWRF runs through 1 model sol on 32 processors in 1 h.

We have compared simple results from our MarsWRF simulations to those of the LMD GCM (Lefèvre and Forget, 2009) and find that MarsWRF reproduces the seasonal polar enhancement of methane of the LMD GCM quite well, and, likewise, does not show a diurnal cycle in methane. Simulations discussed in Section 3 also find similar rates of mixing of methane in the atmospheres of both models. Overall, the behaviors of the LMD and MarsWRF GCMs are quite similar, and should be expected to yield broadly comparable results for similar initial conditions.

## 3. Basic concepts for the behavior of a plume in the Martian atmosphere

The scales at which real atmospheric motions can occur generally fall below the resolution of most numerical models and, given even an initial condition perfectly identical to 'reality', model output will ultimately diverge from the truth so as to be unrecognizable. Largely for this reason, our results will be similar to, but not exact simulations of, observations. However, the model can provide useful insights into how plumes develop in the Martian atmosphere depending on the choices of several key parameters identified above—source location, duration of gas emission and intensity of gas emission. Tracer lifetime can also be taken into consideration, however, for model studies on timescales significantly shorter than the chosen tracer lifetime (1000 days), chemical decay becomes negligible. In this section, we explore two different types of sensitivities—those due to the architecture of the MarsWRF GCM itself and those due to atmospheric physics.

For the purposes of these sensitivity studies, we define a reference, 'baseline' plume simulation, the parameters for which (Table 1) are matched to the M09 results. No background abundance is assumed, in line with the M09 observations, which is a different assumption from previous work (Lefèvre and Forget, 2009). Output from the MarsWRF simulation for this baseline case, 5 sols after the release event, is shown in Fig. 1a.

### 3.1. Sensitivity to model spinup

For all simulations, MarsWRF underwent a 'spinup' of 30 sols (i.e. it was run for 30 days before the tracer release), performed in each simulation's 'native' resolution, to eliminate all transient effects due to startup of the model from rest. The selection of 30 sols was essentially arbitrary, but found to be sufficient for this purpose. To test the sensitivity of MarsWRF to the length of this spinup period, we performed a test identical to that in Fig. 1a, but with a 40 sol spinup period. The results are shown in Fig. 1b. Despite the change in spinup duration, the differences between the two simulations are only minor. Thus, we conclude that the model settles into a realistic atmospheric simulation after 30 model sols of run time, and is not critically dependent on the spinup duration.

**Table 1**
Reference simulation conditions.

| Reference simulation conditions | |
|---|---|
| Emission location | (0°N, 310°W) |
| Total tracer mass | $1.87\times10^7$ kg |
| Chemical lifetime | 1000 sols |
| Emission duration | Pulse (one timestep) |
| Observation delay | 5 sols |
| Emission season | $L_s=155^\circ$ |
| Model resolution | $1.25^\circ\times1.25^\circ$ |

### 3.2. Sensitivity to model resolution

The model resolution can have a large influence on the structure of these simulated plumes. Most Mars global circulation models are run on a grid on the order of $5^\circ\times5^\circ$ for computational efficiency. Fig. 1c shows a plume simulation at this coarse resolution. (The simulation was spun up at $5^\circ\times5^\circ$ resolution with all other parameters identical to the reference simulation). Note that the size of the maximum value within the plume distribution can be no smaller than a single grid box so, relative to the simulation in Fig. 1a, the peak signal in the plume distribution in Fig. 1c is larger. A comparison of Fig. 1a and c show a distinct difference in simulated plume structure for these different model resolutions. As model resolution becomes coarser, the effects of numerical diffusion—an artifact of the discrete nature of the model—are more expansive, leading to less accurate simulations. Fig. 1d shows a simulation using the reference parameters, but spun up and implemented on a $2.5^\circ\times2.5^\circ$ grid, with the resulting plume being much closer to Fig. 1a distribution. Based upon these results, we have concluded that the $1.25^\circ\times1.25^\circ$ model grid, which is computationally tractable, provides results that are only minimally sensitive to the choice of model grid.

### 3.3. Sensitivity to atmospheric diffusion

The dispersal of a plume is a combination of the effects of the bulk motion of atmospheric advection and smaller-scale transport, including diffusion. In M09, eddy diffusion was applied in a simple atmospheric model as the *only* source of tracer motion. Here we can assess the relative importance of these two influences on tracer transport by comparing the simulation in Fig. 1a, computed without inclusion of diffusive transport, to a simulation that includes diffusive transport at a level selected by M09 (having a horizontal diffusion coefficient, $K_h=3.2\times10^4\ m^2\ s^{-1}$). Fig. 1e shows the relative change in plume distribution due to the inclusion of diffusive transport for plumes 5 sols after gas release. Even with large gradients in the plume structure (which occur at the beginning of our simulations, and which maximize the effect of diffusive transport), the results with and without eddy diffusion are quite similar, and differ on the edges of the plume distribution by ~10% or a few ppb at most. As time evolves, the importance of diffusion will decrease, as the plume becomes better mixed in the atmosphere, and concentration gradients are weakened; hence,

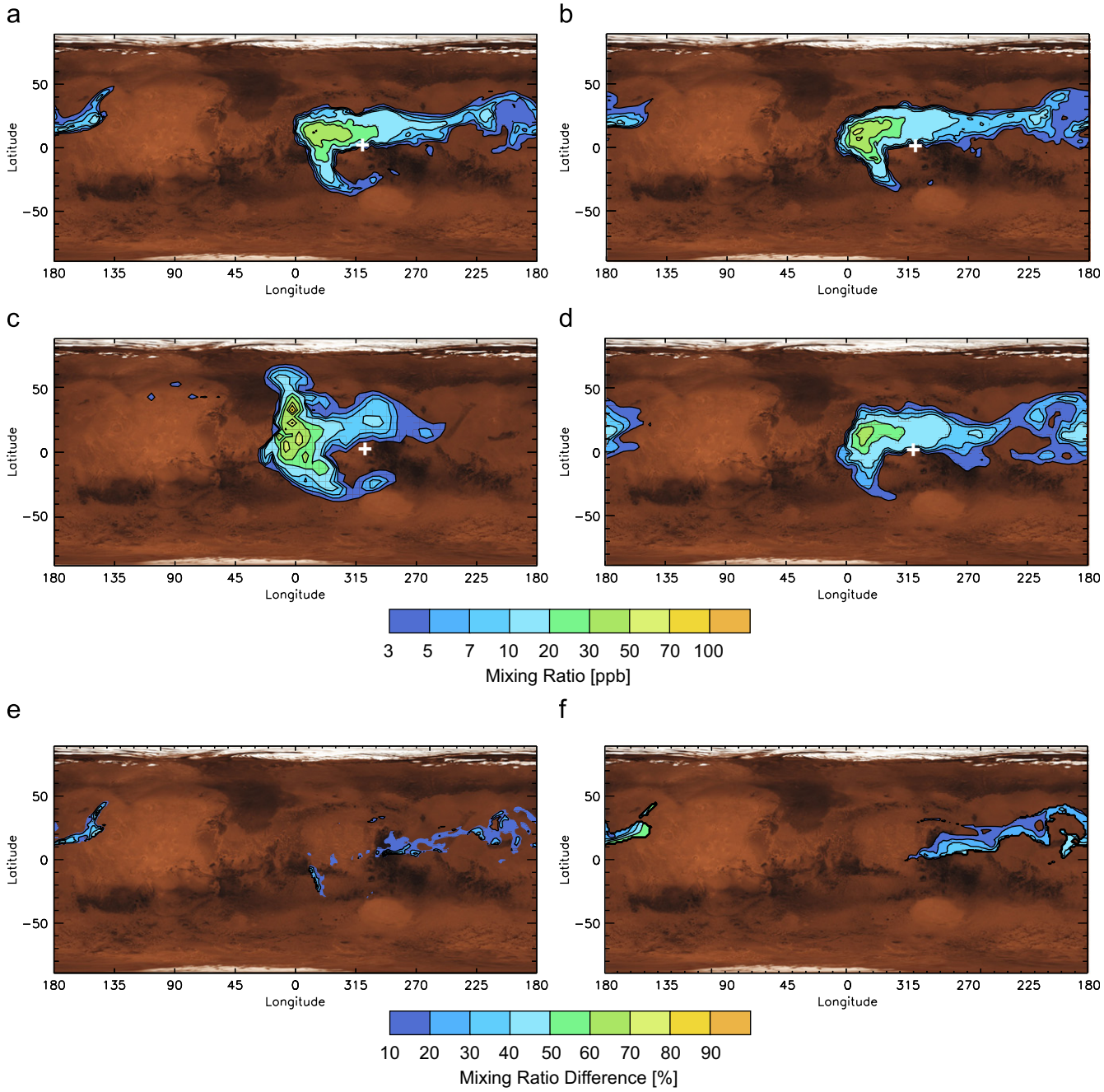


**Fig. 1.** (a) Plume distribution 5 sols after a pulse emission occurred. Simulation parameters listed in Table 1. Contours of the plume intensity show column averaged mixing ratio in ppb. White cross at (0°N, 310°W) indicates source location of the plume. (b) Same as panel (a), but with a 40 sol spinup instead of 30 sol. (c) Simulation for a $5^\circ \times 5^\circ$ model resolution, all other simulation parameters the same as in panel (a). (d) Simulation for a $2.5^\circ \times 2.5^\circ$ model resolution, all other simulation parameters the same as in panel (a). (e) Differences between the strength of a plume from a simulation including both diffusive and advective transport and the strength of a plume from a simulation including only advective transport. Contours only plotted when values from both simulations are $>3$ ppb. Simulation parameters are as in Table 1. (f) Differences between the strength of a plume from a simulation with tracer distributed throughout the first atmospheric scale height at the time of injection and the strength of a plume from a simulation in which the tracer is emplaced just in the first layer. Contours only plotted when values from both simulations are $>3$ ppb. Simulation parameters are as in Table 1.

diffusion appears to play only a small role in the development of these plumes, and cannot be considered the primary mechanism behind plume development as was assumed in M09.

### 3.4. *Sensitivity to vertical distribution of gas release from surface*

In simulations to this point, we have assumed a mild release event, (e.g. a surface seepage), rather than a more explosive-type release, such as from volcanic eruption, which would inject methane to higher altitudes. We further assume that the entire quantity of released tracer is initially placed only into the lowest model layer, as might be expected from a slow event occurring on timescales much longer than a model timestep. More violent releases, however, may throw material much higher into the atmosphere much more quickly than vertical mixing otherwise would. We have explored how tracer injection to higher altitudes can affect the structure of a plume by modifying the initial vertical distribution to inject the tracer at a uniform relative abundance through the first scale height ($\sim$11 km, Fig. 1f) as well as

uniformly throughout the entire vertical column (~80 km, not shown). In both cases, the results show little difference from the surface layer-only distribution in Fig. 1a. There is minimal difference between surface emplacement of tracer and distribution over first scale height since changes in the boundary layer over the diurnal cycle result in rapid vertical transport in the first scale height within 1–2 sols. Higher values around 150°W indicate somewhat more rapid transport of the leading edge of the tracer when well mixed at higher altitudes. As even the uniform distribution up to 80 km still has most of the mass situated in the lower atmosphere, the lower model layers will be the primary drivers of the tracer distribution and will carry the most tracer mass. Therefore, it does not appear from our tests that our results are particularly sensitive to the initial vertical distribution of the tracer.

### 3.5. *Sensitivity to duration of gas release from surface*

As seen in Fig. 1a, the maximum in the plume distribution resulting from a near instantaneous surface gas release is west of the actual source location (indicated by a white cross) as a result of regional easterly winds. This highlights that the maximum plume signal in the atmosphere derived from a surface release need not directly correspond to the location of the surface source.

Fig. 2 shows how the reference plume evolves at even later times after the gas release—further progression in the local plume maximum away from the source location and rapid dispersal of the overall plume volume due to the strong global circulation. For < 20 sols, there is a distinct local maximum in plume intensity, but beyond 20 sols the coherent plume structure is lost, and by 30 sols, an individual plume is no longer identifiable. Note that the mixing ratio at the plume maximum decreases over time as the plume is dispersed (for the selected chemical lifetime of 1000 sols, decrease in mixing ratio cannot be significantly attributed to chemical decay). Therefore, a plume resulting from a (near-) instantaneous gas release will retain its coherent structure only for a period of a few sols and the maximum value will steadily decrease (to ensure mass conservation) as the plume expands in size and becomes well mixed.

Rather than assuming that the gas emission is (near-) instantaneous, the release of the same mass of gas could have occurred over an extended period. If one assumes that the total amount of tracer released is the same in either an instantaneous or extended emission event, there is a direct relationship between the maximum mixing ratio in the plume and the duration of tracer release. To explore this point, we consider a plume in which the same mass of gas is released uniformly over a 10 sol period. Fig. 3 shows this plume both 5 and 10 sols after the start of plume release. Throughout the period of gas release, the point of maximum intensity within the plume is collocated with the surface source position. However, this maximum value can move away from the surface source location as soon as the gas release ends. The total tracer mass in the Fig. 3b plume is equal to the total tracer mass in Fig. 1a (minus a nominal fraction that has decayed in the 10 sol release period) and roughly twice as great as the mass in Fig. 3a. The shape of the plume remains the same regardless of an instantaneous or extended gas release; however, the distribution within the plume itself will differ. At the distal

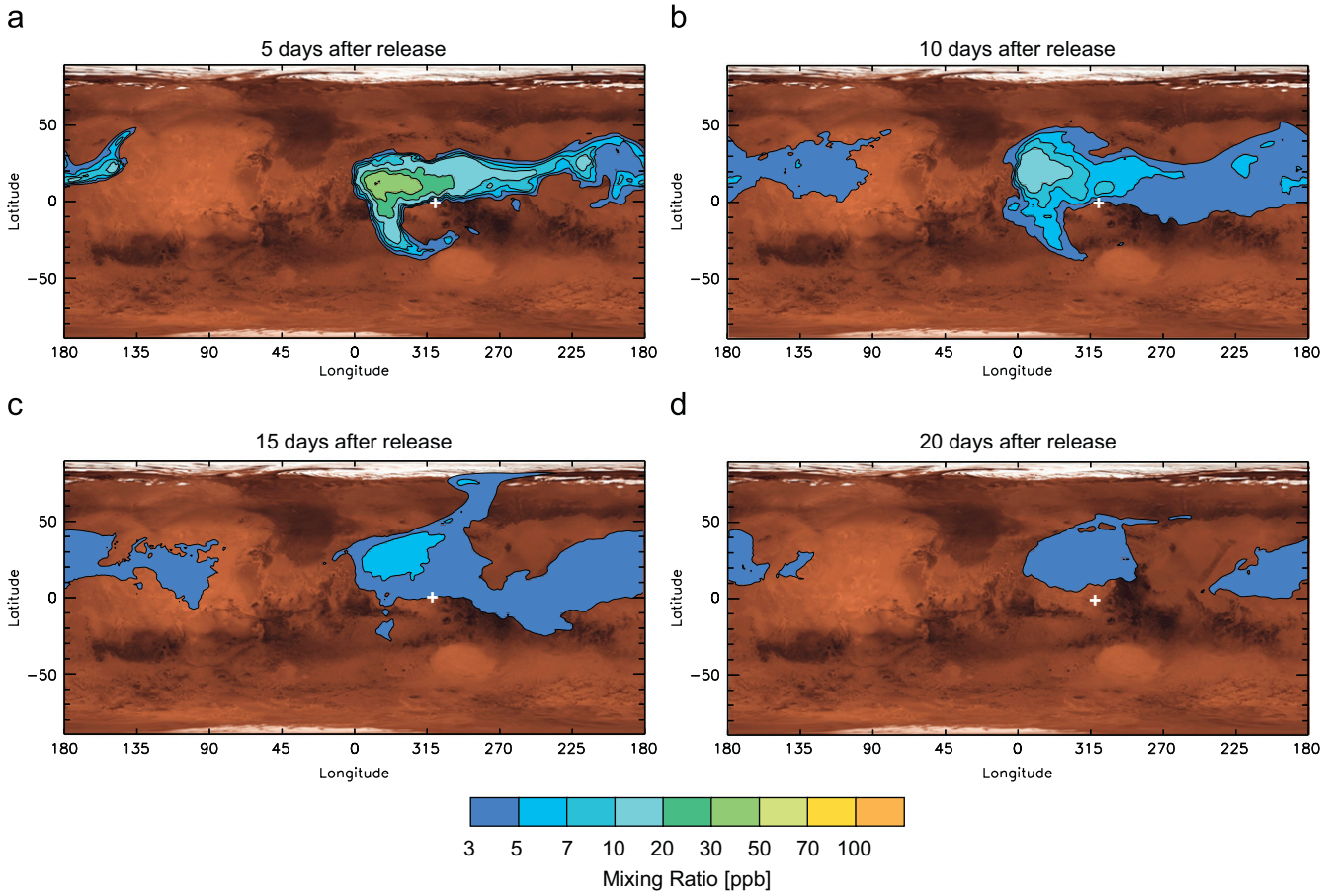


**Fig. 2.** All conditions same as the reference point source 'pulse' emission (Fig. 1a), but for longer times after the moment of gas emission: (a) 5 sols (same as Fig. 1a), (b) 10 sols, (c) 15 sols, (d) 20 sols. Beyond 20 sols, column integrated mixing ratio everywhere falls below the lowest contour at 3 ppb.

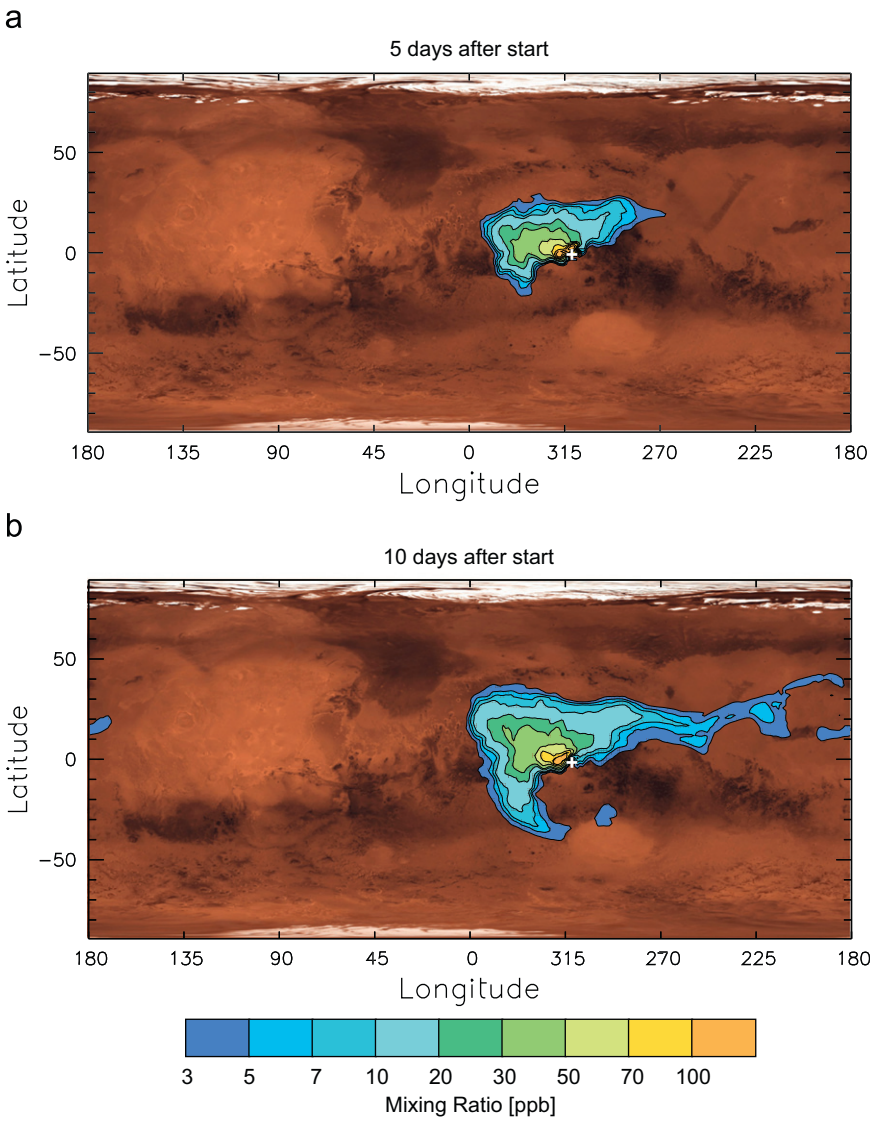


**Fig. 3.** The same conditions as Fig. 1a except that the gas is emitted uniformly over a 10 sol period. The plume (a) 5 sols and (b) 10 sols after the onset of gas release.

edges of the plume (corresponding to the earliest, or 'oldest' released gas), the pulse event will have a stronger signal than the slow release, since, for the latter, only a fraction of the total mass has been released at the start (e.g. only one-tenth of the gas has been released after the first sol). At the core of the plume, where the 'newest' released gas is found, the peak signal for the slow release is about an order of magnitude lower than the peak signal for the pulse event immediately following release.

### 3.6. *Sensitivity to surface location of gas release*

Since topography can affect atmospheric motion near the surface, plume structure can vary dramatically depending on the location of the surface from which the gas is released. Fig. 4 illustrates significant changes to the plume shape resulting from varying source location. As we progressively shift the plume source 'upwind' in Fig. 4a and b (the prevailing winds at the equator in these simulations are easterlies), the resultant plume (after 5 sols) appears to drift strongly to the southeast rather than to the west, as in the baseline simulation. A look at the wind field in Fig. 5 explains why; east of ~270°W, the low level winds shift noticeably to the northwest, which transport the plume generally southward until it gets picked up by the strong westerly flow in the southern mid-latitudes.

Similar sensitivity to source latitude can be seen in Fig. 4c and d, where the latitude of the baseline emission is varied north and south by 15°. Fig. 4c shows that the path of the plume is strongly influenced by Tharsis at this latitude (in Fig. 4c we begin to see the motion of the plume as it curves northward around Olympus Mons). This particular season ($L_s$=155°) is approaching equinox, and two jets of similar strength manifest themselves in the mid-latitudes of each hemisphere. By pushing the plume source location further poleward, this increases the overall likelihood of the tracer signal getting entrained in the stronger westerly jets. This appears to be the situation in the north, while in the south, smaller-scale wind patterns appear to be controlling the plume, keeping it largely fixed at ~330° longitude with a tail to the east, possibly the result of entrainment in the southern hemisphere jet.

Clearly, these results are dependent on our choice of parameters used in MarsWRF; small changes to those values can yield different results. However, the value of the GCM for this study is not in identifying the exact source location of the methane—such an 'inverse' modeling approach may be

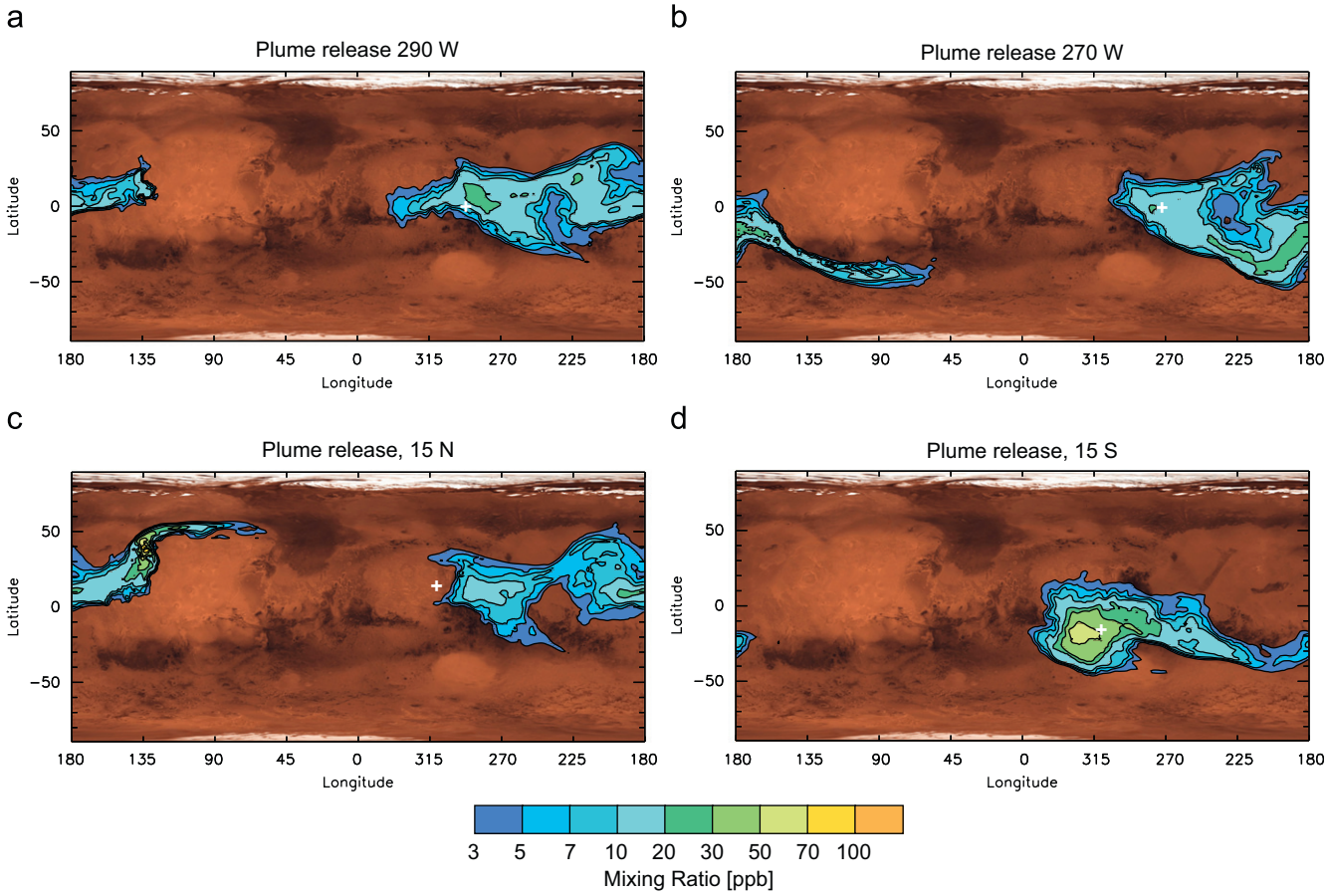


**Fig. 4.** Simulation for surface location of pulse emission where source is (a) 0°N, 290°W, (b) 0°N, 270°W, (c) 15°N, 310°W, (d) 15°S, 310°W. All other simulation parameters are the same as in Fig. 1a.

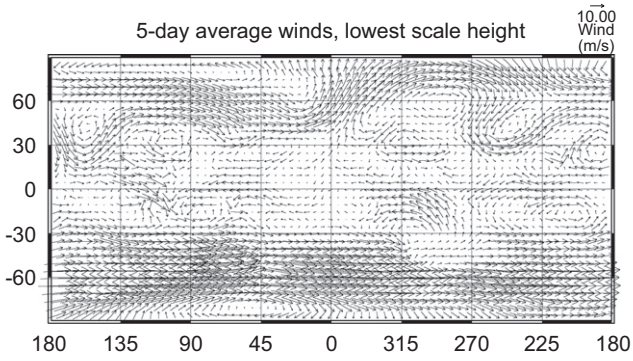


**Fig. 5.** Five-sol average wind field in the lowest scale height at $L_s$=155–157°.

non-unique. Rather, we can garner from the model a set of restrictions on the timing, position and duration of the release event relative to the observation.

## 4. Modeling methane signals on Mars

The results thus far provide a framework for reproducing the methane observations reported by M09. The present work reflects a more detailed analysis of earlier results by Allen et al. (2009) and Mischna and Allen (2009); although some details have changed, the general emission scenario presented in these earlier studies is supported by this most recent work.

The specific observations we seek to match with this technique are illustrated in both Fig. 2c, curve 'd' and Fig. 3 of M09, the latter providing a higher resolution spatial (lat × lon) map of the observed plume. In reproducing these observations with MarsWRF we strive to simultaneously match the values of several parameters:

1. Peak signal: the peak value for the methane mixing ratio in curve 'd' is $\sim 45 \pm 10$ ppb.
2. Plume size: the full-width half-maximum (FWHM) of the curve 'd' signal is approximately 60° in latitude. Additional measurements by M09 further suggest that the plume has a $\sim$60° FWHM signal in longitude.
3. Plume location and season: the strongest portion of the plume (M09 Fig. 3) is centered at (0°N, 310°W) and observations were made between $L_s$=154.5° and 155.0° over two consecutive days (19–20 March 2003). The profile shown in M09 Fig. 2b and c (curve 'd') are a best fit of the 2 sols' observations.

Several assumed parameters derived from M09 will be used as constraints for test model plumes. First, we adopt a methane loss timescale of 1000 sols, which falls in the middle of the 0.6–4 Earth year methane lifetime estimated by M09. For simulation timescales $\ll$1000 sols, then, only a very small fraction of the total methane in the plume, will be lost by chemical decay. So long as the assumed chemical lifetime is long compared with the transport timescales, variations in the assumed methane lifetime will not result in a significantly different plume development.

We have shown, in Fig. 1a, the evolution of a point source pulse plume, released at (0°N, 310°W) after 5 sols, this being our

'simplest', reference model. Remapping these data at the resolution of the M09 observations (16° × 10°, lon × lat) reveals several interesting effects of the observational resolution. The coarser resolution of Fig. 6 reduces the peak observed signal strength from 51 to 42 ppb (cf. Fig. 1a). By the sixth sol after release, the peak signal has fallen below the lower limit of the M09 observed strength (Fig. 7). Thus, we can conclude, from even this most conservative case (we say 'conservative', as a point source pulse will introduce the strongest initial signal into the atmosphere), that the methane observations must take place less than ~6 sols after the methane release, given the assumed release mass of M09. It is clear that as we spread out this release, either in time or space, the plume strength will be diluted, and the timeframe over which the peak signal remains consistent with the M09 observations will be consequently shortened.

A second point to reiterate about the baseline plume in Figs. 1a and 6 is that the peak signal strength appears downwind of the release point, for reasons discussed in Section 3. This indicates that in our model atmosphere, the source location of the plume cannot be at 310°W. Finally, a measure of the FWHM signal in Fig. 6 shows its north–south (N–S) dimension to be much too narrow to be consistent with the M09 observations. Simply, after ~5 sols, the plume has not had sufficient time to amply disperse in the N–S direction, (meridional winds are weaker than zonal winds).

It seems unlikely, then, that the M09 observed plume distribution is the result of a point source emission, as it is difficult to 'grow' a plume with a 60° FWHM from a point source during this season and in this region because of the weak meridional winds. While it is possible to obtain a plume with such a N–S dimension from a point source, such a pattern will only be obtained after perhaps 10–20 sols, by which time the plume has dispersed zonally and the plume peak strength diminished well below the observed values. Consequently, we are led to consider a more expanded source region for the methane.

With dimensions and location for an extended source region as variables, a good fit to the observations was ultimately obtained through trial and error. However, a few constraints can be imposed, a priori, to minimize the search space. A N–S dimension roughly comparable to the N–S width of the observations is likely required to ensure an appropriate size. Given knowledge of the prevailing winds during this season and observation location from the GCM, we can predict a source region upwind of the observations, i.e., not necessarily at the observation longitude. A look at Fig. 5 shows us that, for this particular simulation, at the central longitude of the methane observations there is an eddy in the northern hemisphere with winds blowing west to east, and a general westward trend to the winds in the southern hemisphere. This provides guidance as to where we might place our source relative to the central observation longitude (310°W) in our model simulation. These winds are, of course, model dependent, especially at the smaller scales.

Fig. 8 illustrates our best-fit solution to the M09 methane observations with the aforementioned constraints taken into consideration. The parallelogram shows the approximate dimension of the source region (80° × 15°), which is substantially larger than the point source used for Fig. 1a, and is skewed 'counterclockwise' to account for the latitude-dependent winds seen in our model. As the release region is now substantially larger than the baseline point source, the initial peak signal will be weaker, and a peak value matching curve 'd' in M09 occurs much more quickly—in our best-fit case in as little as 2 sols after release. Taking a slice averaged over 16° longitude (as in M09) through the peak methane signal at 315°W (Fig. 8b) shows our methane profile compares well with the M09 observations (again, centered at 310°W).

The results presented here serve a complementary function to those of Lefèvre and Forget (2009), and the respective approaches

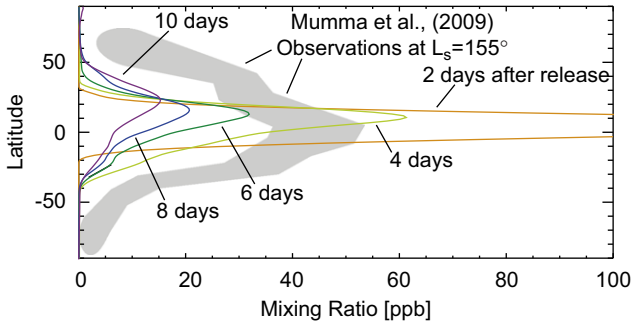


**Fig. 7.** Latitudinal distribution of plume mixing ratio as a function of time for central longitude of 315°W, and 16° × 10° (lon × lat) smoothing. Each curve (progressing from right to left) shows the variation in 2 sol increments, from 2 sols after a 'pulse' release (rightmost) to 10 sols after (leftmost). The shaded region encloses the M09 methane observations (M09, Fig. 2c).

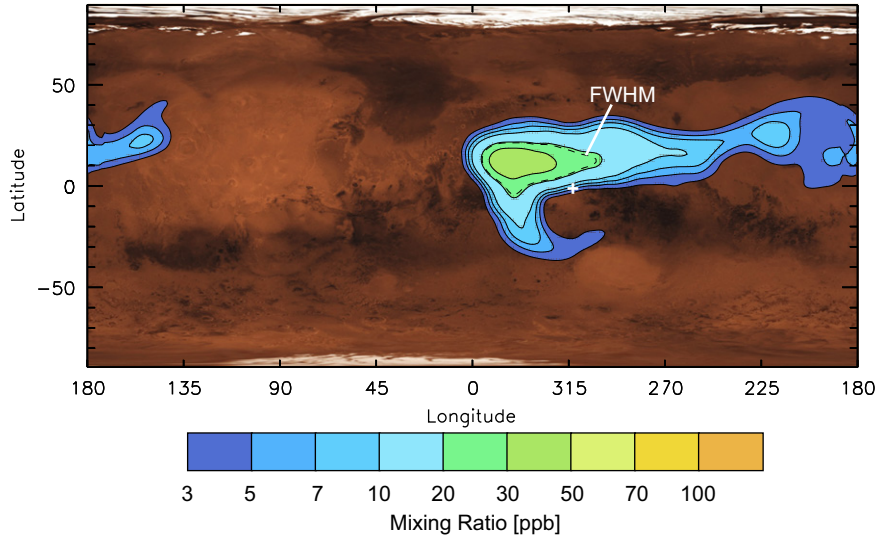


**Fig. 6.** Same as Fig. 1a, but smoothed to a resolution of 16° × 10° (lon × lat) to match the resolution of the M09 observations.

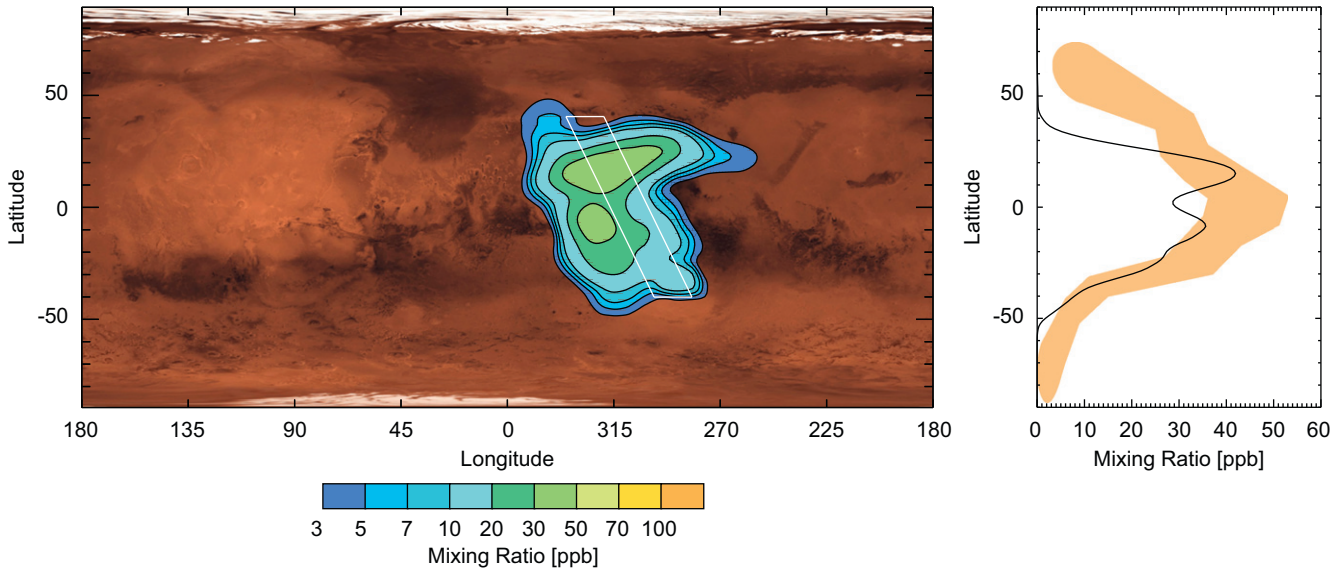


**Fig. 8.** Left: optimal simulation of the M09 observations at $L_s = 155^\circ$ obtained using an extended source of $80^\circ \times 15^\circ$ (lon × lat) in size, skewed counterclockwise from N–S (parallelogram outlines source zone). Right: plume strength (in ppb) along a slice through 315°W (black line) compared with M09 methane observation (M09, Fig. 2c, curve 'd'). Simulation smoothed to $16^\circ \times 10^\circ$ resolution.

differ in two significant ways. In the present work, we assume no background methane abundance, while in Lefèvre and Forget (2009), a steady-state value of 10 ppbv is imposed. The choice of 10 ppbv was selected as an approximation of the mean methane abundance of 14 ppbv in Geminale et al. (2008) (Lefèvre, personal communication). The present choice of zero methane was selected to represent the observed methane abundance outside the plume regions of M09 (with a detectability limit of 3 ppbv). Additional tests (not shown) with a background 10 ppbv methane abundance do not alter the present findings, as the FWHM of the M09 plume is substantially larger than this value, and minimally influenced by a uniform background signal.

The second difference between the present work and Lefèvre and Forget (2009) is the duration and magnitude of the emission event. Here, we have selected a total methane mass equal to the observed plume magnitude in M09 (~19,000 t) and released it in a brief pulse. In Lefèvre and Forget (2009), the total methane mass is equal to their calculated annual photochemical loss of methane (260 t) released over a finite period (60 or 120 days). The initial assumptions, then, are quite different. The two studies address different mechanisms for plume formation—based on a more steady-state emission and an instantaneous release, respectively.

The best-fit conditions obtained in Section 4 seem rather remarkable—the observations would need to be taken almost immediately after a methane release episode, an occurrence that may itself be a rare or unique event. Alternatively, such releases may be commonplace, although they have failed to be detected by other capable orbital and ground-based assets. We make no inferences about the likelihood of this sequence of events taking place.

## 5. Discussion

Additional information can be extracted from the individual daily observations of the strongest methane plume in M09 Fig. 2c. The daily data for these observations are plotted in Fig. 2b of M09 and were obtained on 2 consecutive sols (Fig. 2c, curve 'd' illustrates the 'best fit' to the 2 sols of observations). Differences in the 2 sols of data should reflect not only spatial, but temporal variations in the methane signal as well. The relative strength of the M09 observations (the R0 line on 19 March, 2003, and the R1 line on 20 March, 2003) suggests an *increase* in plume strength with time, a finding which was interpreted by M09 as being a consequence of the second sol of observations being nearer the source location, thus yielding a stronger signal. The possible evolution of the plume in the time between observations is, however, not explicitly noted. The plume is assumed to maintain a static pattern over the 1 sol span between observations, while the changing position of the observations themselves reflects a moving 'window' over this fixed plume. As before, our modeling results suggest that the temporal evolution (i.e. growth) of the plume cannot be neglected on even this timescale. Fig. 9 shows the spatial extent of the best-fit methane plume as in Fig. 8, but with a greater level of smoothing (46° in longitude versus 16°) to match the coarser longitudinal resolution of the data in M09 Fig. 2b. The right-hand panel captures the moment of our best-fit solution, 2 sols after plume release, while the left-hand panel shows the plume 1 sol earlier, simulating the development of the plume over the 1 sol span between the two M09 observations. There is a noticeable growth in the size of the plume, even within a single sol and the peak signal strength diminishes, correspondingly, between the two panels. Fig. 10 reproduces the M09 Fig. 2b results for our best-fit scenario from Fig. 8, and shows the overall decrease in plume strength between the two sets of observations taken 1 sol, and 12° in longitude, apart. (Mars rotates beneath the Earth ~12° each day, shifting the central mean longitude between observations by this amount. Our choices of longitude here straddle our 'best-fit' longitude of 315° from the model results in Fig. 8.) These results differ from those in M09, but this is a consequence of our different approach to plume growth. Our findings with a realistically developing plume show that the weakening of the plume with time will have a greater impact on the relative strength of a particular pair of observations than their location.

The M09 interpretation of the differing R0 and R1 strengths cannot be discounted outright, however, and is plausible under certain specific conditions. Most importantly, the duration of the emission event would have to span the two observations, and the plume be therefore 'fixed' to a specific surface position during this time period. This circumstance could indeed result in a stronger signal on the second sol if the second set of observations lie more

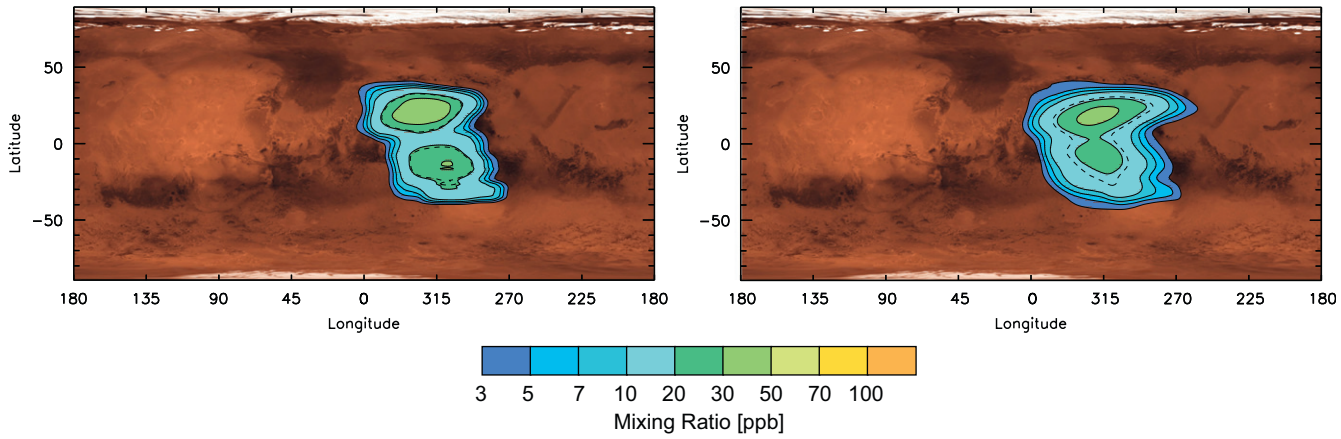


**Fig. 9.** Illustration of the growth of the 'best-fit' plume over 1 sol. Plume source is the parallelogram in Fig. 8. The right panel is the same as Fig. 8, but smoothed to resolution of $46^\circ \times 10^\circ$ (lon × lat).

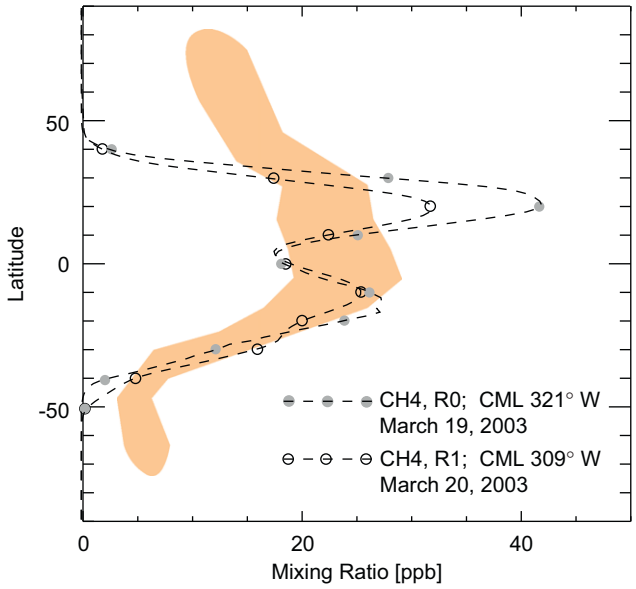


**Fig. 10.** Plume strength, smoothed by 46° in longitude 1 sol (line R0) and 2 sols (line R1) after release. Shaded region is the same as M09 Fig. 2b for reference.

directly above the source point. However, as we have noted, extending the duration of emission while holding the total mass of methane fixed results in a weaker peak signal, and would yield an even shorter time between the emission event and observations—perhaps as little as a few hours.

Overall, the shape and magnitude of the observed methane distribution requires invocation of a large initial source region and other 'special' initial conditions such as the source region orientation. Such a large source region (80° in latitude, or approximately 4700 km) does not match up to any observable surface features such as cracks or rifts in the region, and there is no obvious subsurface process that would produce gas emissions temporally correlated over such a distance and be a likely methane source.

## 6. Conclusions

Based upon a thorough exploration with a general circulation model, we have been able to provide constraints on the nature of the source for the methane observations acquired by Mumma et al. (2009). Any plume that retains the shape and strength of their observed signal and is derived from a total methane mass of $1.87 \times 10^7$ kg must have been released just before the time of observation—no more than 1–2 sols earlier. The total N–S extent of the plume also requires a broad, meridional source rather than a point emission, and must have been derived from a near-instantaneous release event rather than a slow, steady emission.

This approach demonstrates a technique by which we can apply the capabilities of GCMs to localize plume source regions, especially given observational estimates of plume mass and size, which are strong restrictions on the potential age of the plume. It must be stressed that we make no assertion that in this particular solution we have unequivocally identified the source region of the observed plume—we merely illustrate the general characteristics of the source region required to match the M09 observations (i.e. a pulse from a large source region modified to accommodate the prevailing winds, and extremely young).

We have demonstrated the importance of properly considering atmospheric motion when attempting to link source to observation, and that it is unlikely that the source location is coincident with the observed plume maximum unless the plume source is continuously active. These initial modeling results can be used to better develop techniques for isolating potential source locations as the number of observations, and total global coverage increase.

## Acknowledgements

The simulations presented in this paper were performed on the supercomputing clusters at both JPL and the Caltech Division of Geological and Planetary Sciences. Work by M. Mischna and M. Allen was performed at the Jet Propulsion Laboratory, California Institute of Technology, under a contract with the National Aeronautics and Space Administration. We wish to acknowledge stimulating discussions with Mike Mumma, Kevin Zahnle and François Forget on earlier versions of this research. Two anonymous reviewers helped to clarify the story and provided excellent feedback.

## References

Allen, M., Mischna, M.A., Richardson, M.I., Newman, C.E., Toigo, A.D., 2009. Implications of methane plumes in the Martian atmosphere. 41st DPS Meeting, Bulletin of the American Astronomical Society, 41 (3), #44.03.

Christensen, P.R., 25 co-authors, 2001. Mars global surveyor thermal emission spectrometer experiment: investigation description and surface science results. Journal of Geophysical Research 106 (E10), 23823–23871.

Forget, F., Hourdin, F., Fournier, R., Hourdin, C., Talagrand, O., Collins, M., Lewis, S.R., Read, P.L., Huot, J.-P., 1999. Improved general circulation models of the Martian atmosphere from the surface to above 80 km. Journal of Geophysical Research 104 (E10), 24155–24175.

Formisano, V., Atreya, S., Encrenaz, T., Ignatiev, N., Giuranna, M., 2004. Detection of methane in the atmosphere of Mars. Science 306, 1758–1761.

Geminale, A., Formisano, V., Giuranna, M., 2008. Methane in Martian atmosphere: average spatial, diurnal, and seasonal behaviour. Planetary and Space Science 56, 1194–1203.

Held, I., Suarez, M.J., 1994. A proposal for the intercomparison of the dynamical cores of atmospheric general circulation models. Bulletin of the American Meteorological Society 75, 1825–1830.

Hourdin, F., 1992. A new representation of the absorption by the $CO_2$ 15-μm band for a Martian general circulation model. Journal of Geophysical Research 97 (E11), 18319–18335.

Krasnopolsky, V.A., 2007. Long-term spectroscopic observations of Mars using IRTF/CSHELL: mapping of $O_2$ dayglow, CO, and search for $CH_4$. Icarus 190, 93–102.

Krasnopolsky, V.A., Maillard, J.P., Owen, T.C., 2004. Detection of methane in the Martian atmosphere: evidence for life? Icarus 172 537–547.

Lefèvre, F., Forget, F., 2009. Observed variations of methane on Mars unexplained by known atmospheric chemistry and physics. Nature 460, 720–723.

Mischna, M.A., Allen, M, 2009. On the lifetime and extent of methane plumes on Mars. EOS Transactions AGU, 90 (52), Fall Meeting Supplement, Abstract P43C-1439.

Mischna, M.A., Wilson, R.J., 2008. The Mars general circulation model intercomparison study. The Mars Atmosphere: Modeling and Observations Workshop Abstract #9088, Williamsburg, Virginia.

Mumma, M.J., Villanueva, G.L., Novak, R.E., Hewagama, T., Bonev, B.P., DiSanti, M.A., Mandell, A.M., Smith, M.D., 2009. Strong release of methane on Mars in northern summer 2003. Science 323, 1041–1045.

Putzig, N.E., Mellon, M.T., Kretke, K.A., Arvidson, R.E., 2005. Global thermal inertia and surface properties of Mars from the MGS mapping mission. Icarus 173, 325–341.

Richardson, M.I., Toigo, A.D., Newman, C.E., 2007. A general purpose, local to global numerical model for atmospheric and climate dynamics. Journal of Geophysical Research 112, E09001. doi:10.1029/2006JE002825.

Smith, M.D., Pearl, J.C., Conrath, B.J., Christensen, P.R., 2001. One Martian year of atmospheric observations by the thermal emission spectrometer. Geophysical Research Letters 28, 4263–4266.